AN h-BOX METHOD FOR SHALLOW WATER EQUATIONS INCLUDING BARRIERS*

JIAO LI† AND KYLE T. MANDLI†

Abstract. The shallow water equations provide the basic modeling equations for a number of coastal flooding hazards, such as tsunamis and storm surge. In realistic scenarios, there are often structures important to these flows that have a large extent but small width, including sea walls, berms, and harbor barriers. Explicit time stepping schemes, most often used for the shallow water equations, can then suffer from time step restrictions due to the CFL condition. In this article, we introduce an approach that side-steps these issues by allowing a barrier to have zero-width and to cut a cell arbitrarily without suffering from CFL restrictions. This is done by supplementing existing Riemann solvers and leveraging h-box and large time stepping methods. These methods preserve the properties of the Riemann solver and add negligible cost to the original solvers.

Key words. finite volume, h-box method, conservation laws, shallow water equations

AMS subject classifications. 65M08, 65M12, 35L65

DOI. 10.1137/19M128363X

1. Introduction. Coastal flooding events constitute a major threat to communities along the coastlines throughout the world. Although rare, tsunamis can devastate coastal areas and threaten people and property. The Tohoku tsunami, for instance, caused 15,894 confirmed deaths in 2011. Another threat along the coast is storm surge, produced by water being pushed toward the shore by a storm. Hurricane Sandy in 2012 caused \$67.6 billion in direct damage, and in 2013 Typhoon Haiyan claimed over 6,000 lives in the Philippines (see [23, 19]). As the planet warms, global sea level has also risen and is predicted to be 1 meter in the world-wide mean by the end of the century [20, 24]. Higher sea levels also can cause previously minor floods to become disasters, raising the frequency and severity of the threat from coastal flooding.

Computational modeling of these events as efficiently and as accurately as possible is clearly needed. In this article, we present a method for modeling barriers, such as sea walls, without fully resolving them in the context of the shallow water equations defined in one dimension by

(1.1)
$$h_t + (hu)_x = 0, (hu)_t + \left(hu^2 + \frac{1}{2}gh^2\right)_x = -ghb_x,$$

where h is the depth of water, u the depth-averaged velocity, g the gravitational acceleration, and b the bathymetry or topography. The barriers that are being considered are one tool of many that may be used as possible coastal protection strategies. The motivation for the approach presented arrives from the need to run thousands of scenarios so that probabilistic statements can be generated, optimization can be used, and uncertainty due to the climate can be handled. One of the primary issues

^{*}Submitted to the journal's Computational Methods in Science and Engineering section August 26, 2019; accepted for publication (in revised form) January 11, 2021; published electronically March 24, 2021.

https://doi.org/10.1137/19M128363X

[†]APAM Department, Columbia University, New York, NY 10027 USA (jl4170@columbia.edu, kyle.mandli@columbia.edu).

with accomplishing this is the length scales of common coastal protective barriers commonly considered. These barriers tend to have significant length, stretching over kilometers of the coastline, while being a meter or two across in width. This width makes it difficult, if not intractable, to fully resolve given the aforementioned needs for large ensemble calculations. Instead, the basic premise here is that the barrier will be represented by a set of line segments that can arbitrarily cross the computational grid (see Figure 1a) with widths that are infinitely thin. This leads to a number of problems, such as CFL time step constraints, accurately representing the barrier as a barrier (i.e., the barrier should not be leaky), and conservation.

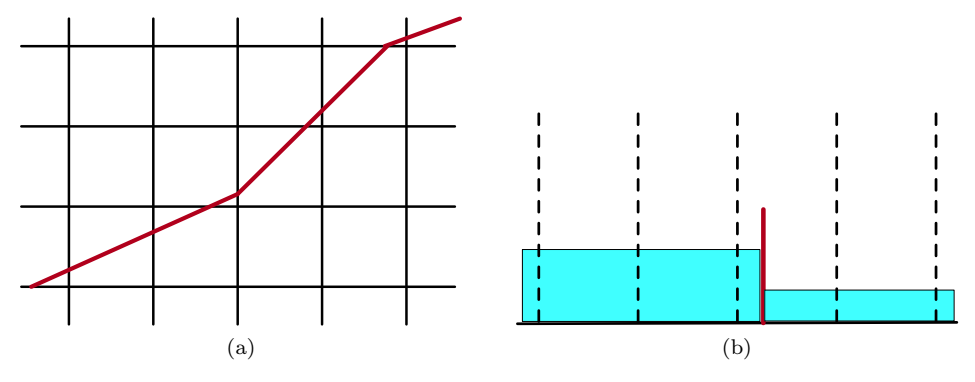


Fig. 1. (a) A two-dimensional example of a barrier (in red) crossing a computational grid arbitrarily. Note the small, nonquadrilateral grid cells that are produced by this. (b) A one-dimensional example of a barrier (in red) crossing a computational grid with grid cells denoted by dashed lines and water columns as blue. This will be the case on which we will concentrate in this article. Color is available online only.

There are a number of alternative choices in the literature for addressing this problem. The most common choice is the use of unstructured grids, which can align with barriers, allowing for simpler flux conditions. Here we maintain that problems such as optimization of a barrier's location would be artificially constrained by an unstructured grid unless such grids were recomputed every optimization step, something that could be extremely costly. Another approach would be to use adaptive mesh refinement (AMR). This would allow the flexibility to place the barriers where needed in an optimization context and allow resolution to be placed dynamically. Fundamentally, however, AMR still requires the resolution of the barrier itself. While this may be feasible in some instances, we still seek an additional approach that may be able to supplement or remove the need to fully resolve these barriers.

We therefore present an approach based primarily on h-box methods and modifications to Riemann solvers that will avoid the difficulties above. The h-box method was originally proposed in a set of papers by Berger and LeVeque (see [4, 5, 7, 8]) that describe a Cartesian grid method for time-accurate solutions of the Euler equations in complex geometries. The primary ideas laid out in these articles center around generating grids that do not follow solid boundaries without special treatment. Instead, these boundaries are embedded into the grid, with no regard for matching grid lines to the body. The h-box method successfully calculates stable fluxes for the resulting cut cells avoiding CFL constrained small cut cells. Later, Berger and Helzel [3] described a simplified h-box method with the perspective of reconstructing larger numerical domains of dependence on a face in such a way that the conservative update on a small cell is formed by fluxes that nearly cancel. All of this work was done in the context of

boundaries that were assumed to be reflecting wall boundary conditions, something that we will need to extend.

In this paper, we present a set of extensions to an existing Riemann solver [15] and numerical techniques for the representation of a barrier that acts as both a reflecting wall boundary condition until it is overtopped and acts as a flux-limiting boundary. Important properties, such as mass and momentum conservation, the barrier preventing flow unless being overtopped, and robustness at the wet-dry interface, need to be preserved. Given the complexity of the problem, this paper will solely focus on the one-dimensional problem. First, the Riemann solver will be extended to handle zero-width barriers at grid cell edges while retaining the desirable properties of the solver. The method will then also be extended to problems where the barrier is not aligned with grid-cell interfaces, taking care to not restrict the time-step due to small cells. This is accomplished by extending existing h-box methods. In section 2, we introduce the form of the finite volume methods used, namely wave propagation algorithms, that will be applied to solve the hyperbolic conservation laws, the basic formulation, and properties of the h-box method and provide a background on subgrid modeling, as well as emphasis on the difficulties that motivate later numerical techniques. Section 3 contains the extensions needed for allowing a zero-width barrier to be used while maintaining key properties of the Riemann solver and extensions to the h-box method that better handle the possibility of water on either side of the barrier. In section 4, numerical results are provided to validate the mathematical methods described. We finally conclude in section 5 with a summary of the results and suggested future directions.

2. Wave propagation and h-box methods. Consider the one-dimensional conservation law

(2.1)
$$q_t(x,t) + f(q(x,t))_x = 0, \quad x \in \mathbb{R},$$

with initial values $q(x,0) = q_0(x)$. For a uniform mesh, the finite volume scheme has the form

(2.2)
$$Q_i^{n+1} = Q_i^n - \frac{\Delta t}{\Delta x} \left[F_{i+1/2}^n - F_{i-1/2}^n \right],$$

where Q_i^n is the cell-average in cell i and time t_n and $F_{i\pm 1/2}^n$ are the numerical flux approximations to the fluxes at the grid cell boundaries. Standard Godunov methods are flux differencing methods (2.2) where exact or approximate solvers are used to determine the numerical flux. The numerical fluxes in a wave propagation method are composed of a set of waves \mathcal{W} that can also be directly viewed as updating the cell that a wave enters. These waves split up the jump in the solution quantities such that

(2.3)
$$Q_i - Q_{i-1} = \sum_{p=1}^{M_w} \mathcal{W}_{i-1/2}^p,$$

along with a set of corresponding wave speeds $s_{i-1/2}^p$, $p=1,\ldots,M_w$. Note that for linear PDEs and approximate Riemann solvers the waves can be defined as scalar multiples of the approximate eigenvectors r^p with $\mathcal{W}^p = \alpha^p r^p$ or simply a projection of the jump onto the eigenspace. Re-averaging these waves onto the adjacent grid

cells, the change of the average value to the right is written as

(2.4)
$$Q_i^{n+1} - Q_i^n = -\frac{\Delta t}{\Delta x} \sum_{\{p: s_{i-1/2}^p > 0\}} s_{i-1/2}^p \mathcal{W}_{i-1/2}^p$$

and to the left as

(2.5)
$$Q_{i-1}^{n+1} - Q_{i-1}^n = -\frac{\Delta t}{\Delta x} \sum_{\{p: s_{i-1/2}^p < 0\}} s_{i-1/2}^p \mathcal{W}_{i-1/2}^p.$$

The net effect in cell C_i is then

$$(2.6) Q_i^{n+1} = Q_i^n - \frac{\Delta t}{\Delta x} \left[\sum_{\{p: s_{i-1/2}^p > 0\}} s_{i-1/2}^p \mathcal{W}_{i-1/2}^p + \sum_{\{p: s_{i+1/2}^p < 0\}} s_{i+1/2}^p \mathcal{W}_{i+1/2}^p \right].$$

As a shorthand notation, we define

(2.7)
$$\mathcal{A}^{-}\Delta Q_{i-1/2} = \sum_{\substack{\{p:s_{i-1/2}^{p} < 0\}\\ \{p:s_{i-1/2}^{p} > 0\}}} s_{i-1/2}^{p} \mathcal{W}_{i-1/2}^{p},$$
$$\mathcal{A}^{+}\Delta Q_{i-1/2} = \sum_{\substack{\{p:s_{i-1/2}^{p} > 0\}\\ \{p:s_{i-1/2}^{p} > 0\}}} s_{i-1/2}^{p} \mathcal{W}_{i-1/2}^{p},$$

so the update (2.6) can then be written as

(2.8)
$$Q_i^{n+1} = Q_i^n - \frac{\Delta t}{\Delta x} (A^+ \Delta Q_{i-1/2} + A^- \Delta Q_{i+1/2}).$$

Note that (2.8) is a more generally applicable approach than the flux differencing approach (2.2), as it can be used in the context of nonconservative hyperbolic PDEs. In the case of a conservation law, if

(2.9)
$$f(Q_i) - f(Q_{i-1}) = \mathcal{A}^- \Delta Q_{i-1/2} + \mathcal{A}^+ \Delta Q_{i-1/2},$$

then the method is conservative. We can also define the fluctuations in terms of the interface fluxes as

(2.10)
$$A^{+}\Delta Q_{i-1/2} = f(Q_i) - F_{i-1/2}, \\ A^{-}\Delta Q_{i+1/2} = F_{i+1/2} - f(Q_i).$$

Adopting the notation described above, (2.9) is equivalent to the requirement

(2.11)
$$f(Q_i) - f(Q_{i-1}) = \sum_{p=1}^{M_w} s_{i-1/2}^p \mathcal{W}_{i-1/2}^p.$$

2.1. The f-wave method. The f-wave method is an alternative way to specify the solution to a Riemann problem. Instead of carrying jumps in the solution Q, we define f-waves \mathbb{Z}^p as carrying jumps in the fluxes such that

(2.12)
$$f(Q_i) - f(Q_{i-1}) = \sum_{p=1}^{M_w} \mathcal{Z}_{i-1/2}^p = \sum_{p=1}^{M_w} \beta_{i-1/2}^p r_{i-1/2}^p,$$

where the latter is again for a linear problem or the result of using an approximate Riemann solver (see [1]). We can also write the relationship between $\mathcal{W}^p_{i-1/2}$ and $\mathcal{Z}^p_{i-1/2}$ if $s^p_{i-1/2} \neq 0$ as

(2.13)
$$\mathcal{W}_{i-1/2}^p = \frac{\mathcal{Z}_{i-1/2}^p}{s_{i-1/2}^p}.$$

As before, some set of speeds $s_{i-1/2}^p$, $p=1,\ldots,M_w$, are associated with the waves. The fluctuations can then be defined by

$$(2.14) \quad \mathcal{A}^{-}\Delta Q_{i-1/2} = \sum_{\{p: s_{i-1/2}^{p} < 0\}} \mathcal{Z}_{i-1/2}^{p}, \quad \mathcal{A}^{+}\Delta Q_{i-1/2} = \sum_{\{p: s_{i-1/2}^{p} > 0\}} \mathcal{Z}_{i-1/2}^{p}.$$

2.2. Source terms. The shallow water equations over nonconstant bathymetry (1.1) require treatment of the source term on the right-hand side of the momentum equation. For convenience, we will write the shallow water equations in the form

(2.15)
$$q_t(x,t) + f(q(x,t))_x = \psi(q,x),$$

where $q = [h, hu]^T$, $f = [hu, hu^2 + 1/2gh^2]^T$, and the source terms are

(2.16)
$$\psi(q,x) = \begin{bmatrix} 0 \\ -ghb_x \end{bmatrix}.$$

We can modify the homogeneous f-wave method described above by incorporating the source term into the flux difference before decomposing it such that

(2.17)
$$f(Q_i) - f(Q_{i-1}) - \Delta x \Psi_{i-1/2} = \sum_{p=1}^{M_w} \mathcal{Z}_{i-1/2}^p = \sum_{p=1}^{M_w} \beta_{i-1/2}^p r_{i-1/2}^p,$$

where $\Delta x \Psi_{i-1/2}$ is some approximation to $\int_{x_{i-1}}^{x_{i+1}} \psi(q,x) dx$. The fluctuations at grid cell interfaces are then defined in the standard way (2.14) where the standard updating formula (2.8) can then be used. For the shallow water equations with bathymetry, it is natural to approximate the source term $\Delta x g h B_x$ at $x_{i-1/2}$ by $\frac{1}{2} g(h_{i-1} + h_i)(B_i - B_{i-1})$, resulting in the vector $f(Q_i) - f(Q_{i-1}) - \Delta x \Psi_{i-1/2}$ taking the form

$$(2.18) \qquad \left[\begin{array}{c} h_i u_i - h_{i-1} u_{i-1} \\ (h_i u_i^2 + \frac{1}{2}gh_i^2) - (h_{i-1} u_{i-1}^2 + \frac{1}{2}gh_{i-1}^2) + \frac{1}{2}g(h_{i-1} + h_i)(B_i - B_{i-1}) \end{array} \right].$$

This vector is decomposed into f-waves, for example, by writing it as a linear combination of the eigenvectors $r_{i-1/2}^p$.

2.3. The *h*-box method. Allowing the representation of barriers to cut arbitrarily through a grid cell brings with it additional challenges. In one dimension, this intersection forms two cells of arbitrary width relative to the rest of the grid. The critical problem then becomes the resulting restriction due to the CFL condition. In the context of our previous definitions, this amounts to the condition

(2.19)
$$\Delta t \max_{i} \left(\frac{\max(\max_{p}(s_{i-1/2}^{p}, 0), |\min_{p}(s_{i+1/2}^{p}, 0)|)}{\Delta x_{i}} \right) \leq 1,$$

where Δx_i is the length of the *i*th grid cell $C_i = [x_{i-1/2}, x_{i+1/2}]$. This can lead to severe restrictions of the time step due to CFL constraints even though only a small handful of cells may have a small effective area.

To combat this restriction one approach is to merge neighboring small cells together, but it has the drawback that this becomes difficult to implement in more complex or higher-dimensional situations [2, 10, 13, 22, 25]. Another alternative is to redistribute the fluxes computed on the edges of the cells that are cut by the barrier. The small cells receive proportionally less flux than a full cell would, and the remaining flux is redistributed to the surrounding cells [9, 11, 21]. In practice, this approach appears to be globally second order accurate but is only first order at the barrier. A broad class of methods that are interpolation based, such as ghost cell schemes, are also possible [12, 14]. Instead, we will utilize the h-box approach to avoid significant CFL restrictions.

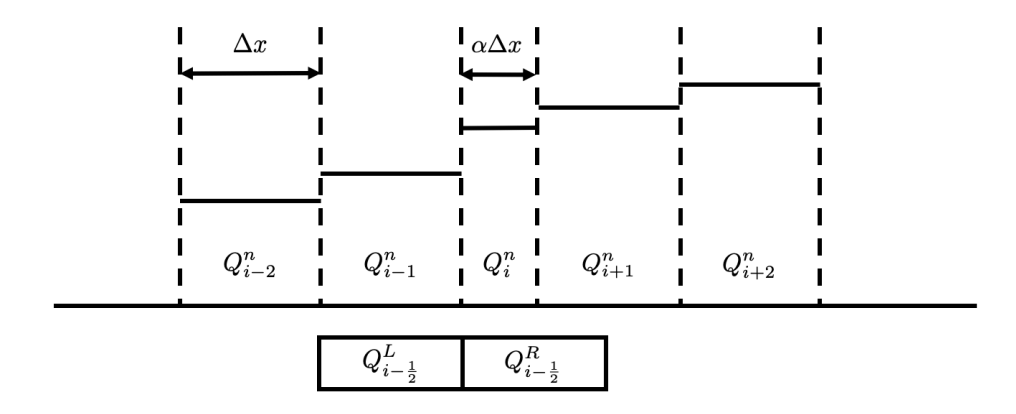


Fig. 2. The model problem in one space dimension has one small cell in the middle of the domain with mesh width $\alpha\Delta x$, $0 \le \alpha \le 1$. The boxes below the axis indicate the h-boxes used to compute the flux at the left interface of the small cell.

In this case, consider the one-dimensional case where the mesh is uniform of width Δx except for one small cell with mesh width $\alpha \Delta x$, where $0 < \alpha < 1$ (see Figure 2). Due to the small cell, the numerical method must be modified in order to satisfy the stability condition (2.19), which may cause limitations on the time steps Δt . Similar in flavor to the merging of small neighboring cells together, we will instead only merge these cells to perform the calculation of the waves. Berger and LeVeque [7] define new left and right states over boxes of length Δx at the edges of the small cell. The basic idea of the h-box method is to approximate the numerical fluxes at the interfaces of a small cell based on states over a region of length Δx , where Δx is chosen as a regular cell size. By construction, the numerical method would remain stable with time steps based on a CFL condition for the regular cells. For the advection equation $q_t + uq_x = 0$, it is easy to prove that the fluxes satisfy a cancellation property [3], such that

(2.20)
$$\mathcal{F}(Q_{i+1/2}^L, Q_{i+1/2}^R) - \mathcal{F}(Q_{i-1/2}^L, Q_{i-1/2}^R) \sim \mathcal{O}(\alpha \Delta x),$$

where $\mathcal{F}(Q^L,Q^R)$ is the numerical flux function. Extending this to nonlinear systems, we use a method of the form

(2.21)
$$\frac{d}{dt}Q_i(t) = -\frac{1}{\alpha \Delta x} \left(\mathcal{F}(Q_{i+1/2}^L(t), Q_{i+1/2}^R(t)) - \mathcal{F}(Q_{i-1/2}^L(t), Q_{i-1/2}^R(t)) \right),$$

where the states Q^L, Q^R are averages over boxes of length Δx extending to the left and right from the cut cell's interfaces. These boxes $Q^L_{i-\frac{1}{2}}, Q^R_{i-\frac{1}{2}}$ are indicated at the bottom of Figure 2 for the cell edge $i-\frac{1}{2}$ to the left of the small cell.

We can then define the solution value of the h-box $Q_{i-1/2}^R$ as the integral average over a box of length Δx ,

$$Q_{i-1/2}^{R} = \frac{1}{\Delta x} \int_{x_{i-1/2}}^{x_{i-1/2} + \Delta x} Q(x) dx$$

$$= \alpha Q_i + (1 - \alpha) \left(Q_{i+1} - \frac{\alpha \Delta x}{2} \nabla Q_{i+1} \right)$$

$$= \alpha Q_i + (1 - \alpha) (Q_{i+1} + (\bar{x} - x_{i+1}) \nabla Q_{i+1}),$$
(2.22)

where the point $\bar{x} = x_i + \frac{\Delta x}{2} = x_{i+1} - \frac{\alpha \Delta x}{2}$ is the centroid of the portion of the integral overlapping cell i+1.

For the first order scheme, setting the gradient $\nabla Q_{k+1} = 0$ reduces to

(2.23)
$$Q_{i-1/2}^{R} = \alpha Q_i + (1 - \alpha)Q_{i+1}, Q_{i+1/2}^{L} = \alpha Q_i + (1 - \alpha)Q_{i-1}.$$

The other two boxes $Q_{i-1/2}^L$ and $Q_{i+1/2}^R$ overlap exactly with a single mesh cell, and the h-box values are simply the cell average for the regular cells. In order to achieve a higher order scheme, we construct $Q_{i-1/2}^R$ using linear interpolation on the grid cells overlapped by the h-box. Applying a backward difference $\nabla Q_{i+1} = \frac{Q_{i+1} - Q_i}{x_{i+1} - x_i}$, the resulting formulas are

(2.24)
$$Q_{i-1/2}^R = \frac{2\alpha Q_i + (1-\alpha)Q_{i+1}}{1+\alpha},$$
$$Q_{i+1/2}^L = \frac{2\alpha Q_i + (1-\alpha)Q_{i-1}}{1+\alpha}.$$

We write the h-box values in a general form

(2.25)
$$Q_{i-1/2}^{R} = \lambda Q_i + (1 - \lambda)Q_{i+1}, Q_{i+1/2}^{L} = \lambda Q_i + (1 - \lambda)Q_{i-1},$$

where $\lambda = \alpha$ for the first order scheme and $\lambda = \frac{2\alpha}{1+\alpha}$ for the second order scheme. The resulting method with a second order (2.24) Lax–Wendroff flux function has been shown in [6] to be second order. In addition, according to the theory in [16], the scheme with the cut cell is stable as $\alpha \to 0$.

Although the h-box method solves part of our problem, it was primarily designed for cases where only one side of a barrier is being considered and a reflective boundary is desired, i.e., $a\ wall$. Unfortunately, as we will see in section 3, we need to modify the h-box method to accommodate more than just a reflecting barrier and use another method to assist in the most complex cases, as the h-box average state that should be used is unknown.

3. A barrier-aware solver for the shallow water equations. In this section, we describe the method proposed for the shallow water equations in the presence of a barrier. The organization of this section starts with the basic method for the simplest

case, one where the barrier is not overtopped and waves are purely reflected off of the barrier. This first case is most similar to the original h-box method and is described in subsection 3.1. The next complexity develops the basics of a barrier that is aligned with the grid and has zero-width but is overtopped by the water on only one side of the barrier so that there is no contrary flow over the barrier (subsection 3.2). The next extension of the solver allows for the barrier to be overtopped from both sides, and therefore the fluid interacts from both sides of the barrier. This is handled by a "ghost fluid" that provides an interaction term between the two fluids on either side of the barrier, detailed in subsection 3.3. Finally, we again consider a barrier that is not aligned with the grid, including all forms of overtopping. Unfortunately, at this point the approach for specifying the ghost fluid is currently unknown, as the states needed are ambiguous, so we instead supplement the h-box approach with a large time-stepping (LTS) method. The advantage of the LTS method is that it does not require the direct use of the ghost fluid outside of what has already been presented, as detailed in subsection 3.4. The final method is therefore a hierarchy of adaptations to the original h-box, which includes the LTS method. This set of modifications and methods is detailed for the reader in Table 1 to help with the admittedly complex hierarchy of methods being described.

 ${\it TABLE~1} \\ Description~of~the~method~presented~here~along~with~each~step~in~the~process's~validity~and~capabilities.$

Name of method	Grid aligned	Overtopping barrier	Section
Augmented h-box	No	No	3.1
Wave redistribution (WD)	Yes	Yes, 1-sided	3.2
WD + ghost fluid (GF)	Yes	Yes, 2-sided	3.3
WD + large time-stepping	No	Yes, 2-sided	3.4

3.1. Augmented h-box method. Consider the model problem shown in Figure 3. A zero-width wall separates the cell into two parts with mesh width $\alpha \Delta x$ and $(1-\alpha)\Delta x$, respectively. We suppose that the wall is high enough to keep the water from overtopping the barrier, and the wall reflects water without mass loss. Then we have

$$Q_{i-1/2}^{L} = Q_{i-1}, Q_{i-1/2}^{R} = \alpha Q_i + (1-\alpha)Q_{i+1}^{\dagger},$$

$$Q_{i+1/2}^{L} = \frac{(1-\alpha)Q_{i-1} + 2\alpha Q_i}{1+\alpha}, Q_{i+1/2}^{R} = \frac{(2-2\alpha)Q_{i+1} + \alpha Q_{i+2}}{2-\alpha},$$

$$Q_{i+3/2}^{L} = \alpha Q_i^{\dagger} + (1-\alpha)Q_{i+1}, Q_{i+3/2}^{R} = Q_{i+2},$$

where

$$Q_i^{\dagger} = \begin{bmatrix} h_{i+1} \\ -h_{i+1}u_{i+1} \end{bmatrix}, \qquad Q_{i+1}^{\dagger} = \begin{bmatrix} h_i \\ -h_iu_i \end{bmatrix}$$

represents the ghost cell values used to represent a reflecting boundary, in this case the wall.

Discretizing (2.21) using the f-wave algorithm and notation, the update in the small cell can be written in the form

$$Q_i^{n+1} = Q_i^n - \frac{\Delta t}{\alpha \Delta x} \left(\mathcal{A}^+ \Delta \hat{Q}_{i-\frac{1}{2}} - f(Q_{i-\frac{1}{2}}^R) - \Psi_{i-\frac{1}{2}}^R + \mathcal{A}^- \Delta \hat{Q}_{i+\frac{1}{2}} + f(Q_{i+\frac{1}{2}}^L) + \Psi_{i+\frac{1}{2}}^L \right),$$

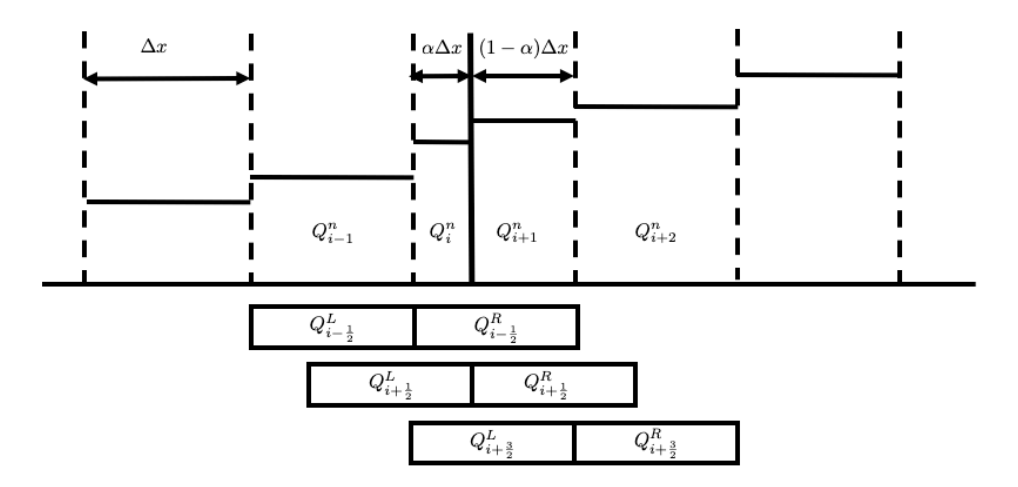


Fig. 3. The model problem in one space dimension has a barrier (solid bold line) separating a cell into two parts with mesh widths $\alpha \Delta x$ and $(1-\alpha)\Delta x$. The boxes below the axis indicate the h-boxes used to compute the flux at the interfaces i-1/2, i+1/2, and i+3/2, respectively.

where

$$\begin{cases} \Delta \hat{Q}_{i-\frac{1}{2}} = Q_{i-\frac{1}{2}}^R - Q_{i-\frac{1}{2}}^L, \\ \Delta \hat{Q}_{i+\frac{1}{2}} = Q_{i+\frac{1}{2}}^R - Q_{i+\frac{1}{2}}^L \end{cases}$$

and

$$\begin{cases} \Psi^{L}_{i+\frac{1}{2}} = \frac{1}{2}g(h^{L}_{i+\frac{1}{2}} + h^{R}_{i-\frac{1}{2}})b^{L}_{i+\frac{1}{2}}, \\ \Psi^{R}_{i-\frac{1}{2}} = \frac{1}{2}g(h^{L}_{i+\frac{1}{2}} + h^{R}_{i-\frac{1}{2}})b^{R}_{i-\frac{1}{2}}. \end{cases}$$

In the limiting case $\alpha=1$, we have $Q_{i-\frac{1}{2}}^R=Q_{i+\frac{1}{2}}^L$ and (3.3) reduces to the first order accurate f-wave algorithm that is valid in the regular parts of the grid. For a system without source terms, $\Psi_{i+\frac{1}{2}}^L$ and $\Psi_{i-\frac{1}{2}}^R$ can be removed and (3.3) reduces to the first order accurate wave propagation algorithm. The formula is valid for linear and nonlinear equations as well as systems of conservation laws, assuming we have a Riemann solver that provides us a decomposition of Q^R-Q^L . If the wall is not high enough to prevent water from passing over, then we resort to other approaches as discussed in subsection 3.2.

3.2. Wave redistribution. In this section, we will first formulate the numerical method that allows water to overcome a barrier. We will also simplify our discussion for the time being to the case where the barrier is aligned with the grid (see Figure 4). This approach also provides a basis for a comparison between a zero-width wall and a wall that has a finite width and in an ideal sense would limit to a zero-width wall. The method also extends the one from subsection 2.3, as it allows water to flow over the barrier and therefore is an extension to the original wall boundary conditions of the h-box method as presented previously. Consequently, properties such as mass and momentum conservation are preserved when appropriate, as well as the well-balancing property and robustness of the wet-dry interfaces.

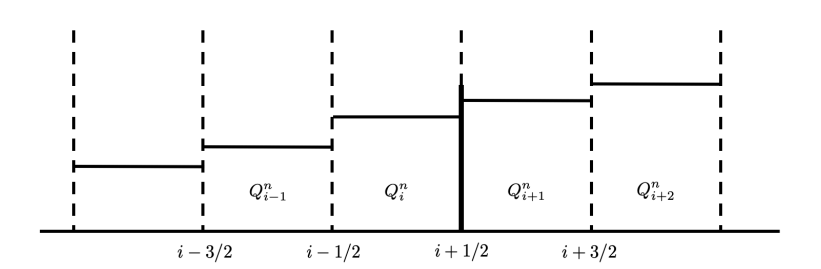


Fig. 4. The model problem in one space dimension has a wall (solid bold line) placed at the edge i + 1/2.

Now that we are allowing water to pass from one side of the barrier to the other, we need to ensure that a Riemann solver handles this eventuality correctly. We can do this by solving additional Riemann problems and modifying the updates the solvers suggest. To enable this, we will employ ghost cells and solve additional Riemann problems using special states that we specify in each of the ghost cells (see Figure 5). These ghost cells will in essence solve a problem as if a finite width barrier was actually present. The resulting solution, however, will result in too many waves. We will redistribute these waves, similar to how other similar methods redistribute fluxes, such that they will impact the original cells on either side of the wall. If carefully done, this will maintain conservation and ensure that water flows from one side of the barrier to the other as determined by the given Riemann solver.

Given the data $Q_{i+1/2}^L$ and $b_{i+1/2}^L$ in cell i and $Q_{i+1/2}^R$ and $b_{i+1/2}^R$ in cell i+1, two ghost cells are constructed to compute the waves $\mathcal{Z}_{i+1/2}^1$ and $\mathcal{Z}_{i+1/2}^2$ shown in Figure 5. A ghost cell with $b_{i+1/2}^{R-1}$ and $Q_{i+1/2}^{R-1}$ is placed at the right of the barrier. The waves $\mathcal{Z}_{i+1/2}^{1-1}$ and $\mathcal{Z}_{i+1/2}^{2-1}$ are computed using the f-wave method. Similarly, a ghost cell with $b_{i+1/2}^{L+1}$ and $Q_{i+1/2}^{L+1}$ is placed at the left of the barrier and waves $\mathcal{Z}_{i+1/2}^{1-1}$ and $\mathcal{Z}_{i+1/2}^{2-1}$ are computed. The proper setting of $b_{i+1/2}^{R-1}$, $Q_{i+1/2}^{R-1}$, $Q_{i+1/2}^{L+1}$, and $Q_{i+1/2}^{L+1}$ will be discussed later. Given the four waves represented by the eigenvectors r^p and scalar wave strengths β^p , we write the waves computed using an f-wave method associated with ghost cells as

(3.6)
$$\mathcal{Z}_{i+1/2}^{1-} = \beta_{i+1/2}^1 r^1, \qquad \mathcal{Z}_{i+1/2}^{2-} = \beta_{i+1/2}^2 r^2, \\ \mathcal{Z}_{i+1/2}^{1+} = \beta_{i+1/2}^3 r^3, \qquad \mathcal{Z}_{i+1/2}^{2+} = \beta_{i+1/2}^4 r^4$$

and the vector **R** and corresponding coefficient vector $\boldsymbol{\beta}$ as

(3.7)
$$\mathbf{R} = [r^1, r^2, r^3, r^4], \qquad \boldsymbol{\beta} = [\beta^1, \beta^2, \beta^3, \beta^4].$$

To derive the redistributed waves as presented in Figure 5, a vector of new coefficients is constructed by adding corrections to the coefficients β^1 and β^4 and setting β^2 and β^3 to zero. Therefore, the waves that we need to redistribute correspond to the second and third eigenvectors leading to the new expression

(3.8)
$$\widehat{\beta} = [\beta^1 + \gamma^1, 0, 0, \beta^4 + \gamma^2],$$

effectively redistributing the waves that are traveling through the ghost cell. Furthermore, given the importance of maintaining conservation, the redistribution of

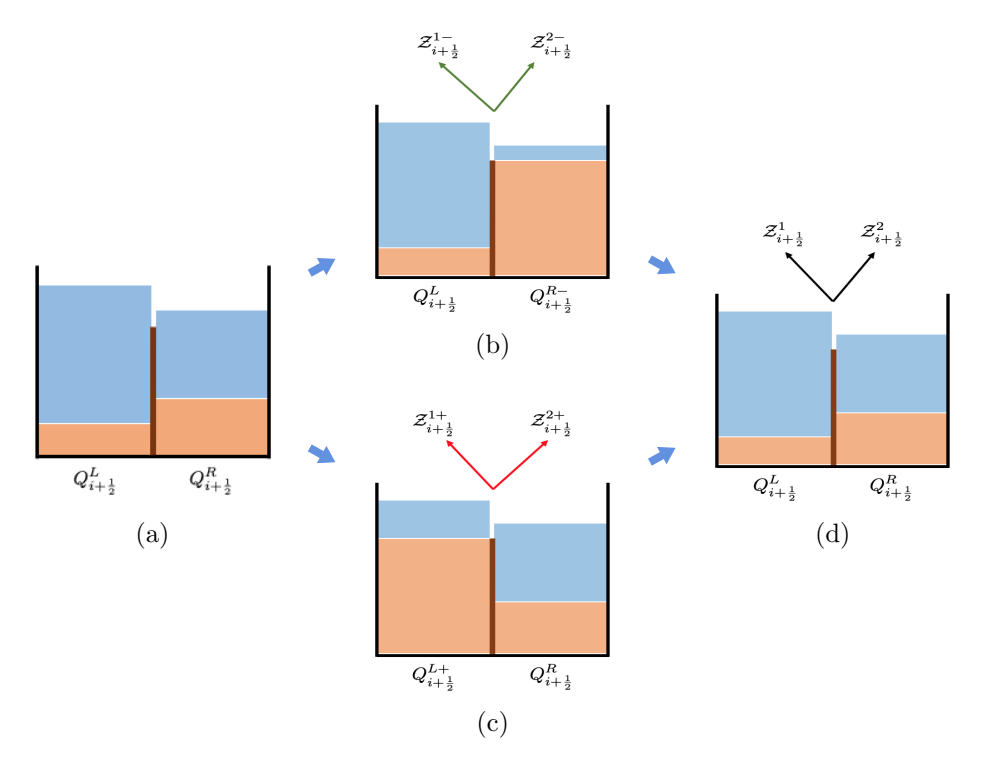


Fig. 5. (a) is a diagram of wave redistribution along the zero-width barrier at the grid cell edge i+1/2. Due to the representation of the barrier, the Riemann solver splits into a new left (b) and right (c) Riemann problem, which are then recombined back into a single Riemann problem in (d) by redistributing the waves as presented in (3.11).

the waves uses conservation to determine the redistribution. This then requires the solution of the system

(3.9)
$$\mathbf{R} \cdot \widehat{\boldsymbol{\beta}}^T = \mathbf{R} \cdot \boldsymbol{\beta}^T.$$

Solving this system leads to the redistribution

(3.10)
$$\begin{cases} \gamma^1 &= \frac{(s^4 - s^2)\beta^2 + (s^4 - s^3)\beta^3}{s^4 - s^1}, \\ \gamma^2 &= \frac{(s^2 - s^1)\beta^2 + (s^3 - s^1)\beta^3}{s^4 - s^1}, \end{cases}$$

where s^p are the speeds of the corresponding waves. We write $\mathcal{Z}^1_{i+1/2}$ and $\mathcal{Z}^2_{i+1/2}$ in Figure 5 as

(3.11)
$$\mathcal{Z}_{i+1/2}^1 = (\beta^1 + \gamma^1)r^1, \qquad \mathcal{Z}_{i+1/2}^2 = (\beta^4 + \gamma^2)r^4.$$

3.3. Ghost fluid. The wave redistribution method is predicated on the desire that we maintain conservation. Up until now, however, we have ignored a couple of critical cases that arise that require setting $b_{i+1/2}^{R-}$, $Q_{i+1/2}^{R-}$, $b_{i+1/2}^{L+}$, and $Q_{i+1/2}^{L+}$. We denote $(\cdot)_{i+1/2}^{L+}$ $((\cdot)_{i+1/2}^{R-})$ as the quantity of the ghost cell on the left (right) to the barrier placed at edge i+1/2. We require that the redistribution is equivalent to the conventional method without the barrier in this limit as the barrier's height goes

to zero. A similar argument for this ghost fluid can also stem from the desire for a well-balanced method but does not cover all cases that we will need.

From (2.17), we can solve the β 's to find

(3.12)
$$\begin{bmatrix} \beta^1 \\ \beta^2 \end{bmatrix} = \frac{1}{s^2 - s^1} \begin{bmatrix} s^2 \delta_1 - \delta_2 \\ -s^1 \delta_1 + \delta_2 \end{bmatrix},$$

where

$$\begin{cases} \delta_1 &= (hu)_R - (hu)_L, \\ \delta_2 &= (hu^2)_R + \frac{1}{2}gh_R^2 - (hu^2)_L - \frac{1}{2}gh_L^2 + \frac{1}{2}g(h_L + h_R)(b_R - b_L). \end{cases}$$

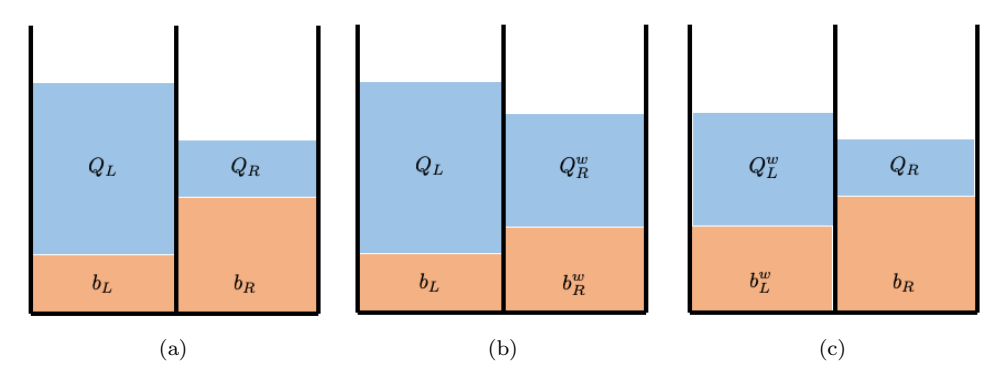


FIG. 6. (a) is a diagram of the conventional f-wave method along the left and right states with bathymetry at the grid cell edge. For the wave redistribution method, the Riemann solver resorts to the left and right sides of the edge in (a) with insertion of a ghost cell as (b) and (c). The superscripts with w represent the ghost cell values placed on the wall.

In this section, we study how the bathymetry impacts the methods being described. The source term is incorporated into the flux difference before decomposing into waves. For Figure 6a, we have

(3.13)
$$\begin{bmatrix} \beta_*^1 \\ \beta_*^2 \end{bmatrix} = \frac{1}{s^2 - s^1} \begin{bmatrix} s^2 \delta_1^* - \delta_2^* \\ -s^1 \delta_1^* + \delta_2^* \end{bmatrix},$$

where

$$\begin{cases} \delta_1^* &= (hu)_R - (hu)_L, \\ \delta_2^* &= (hu^2)_R + \frac{1}{2}gh_R^2 - (hu^2)_L - \frac{1}{2}gh_L^2 + \frac{1}{2}g(h_L + h_R)(b_R - b_L). \end{cases}$$

For Figures 6b and 6c, we have

$$\begin{bmatrix} \beta^1 \\ \beta^2 \end{bmatrix} = \frac{1}{s^2 - s^1} \begin{bmatrix} s^2 \delta_1^L - \delta_2^L \\ -s^1 \delta_1^L + \delta_2^L \end{bmatrix},$$

$$\begin{bmatrix} \beta^3 \\ \beta^4 \end{bmatrix} = \frac{1}{s^4 - s^3} \begin{bmatrix} s^4 \delta_1^R - \delta_2^R \\ -s^3 \delta_1^R + \delta_2^R \end{bmatrix},$$

where

$$\begin{cases} \delta_1^L &= (hu)_R^w - (hu)_L, \\ \delta_2^L &= (hu^2)_R^w + \frac{1}{2}gh_R^{w^2} - (hu^2)_L - \frac{1}{2}gh_L^2 + \frac{1}{2}g(h_L + h_R^w)(b_R^w - b_L), \\ \delta_1^R &= (hu)_R - (hu)_L^w, \\ \delta_2^R &= (hu^2)_R + \frac{1}{2}gh_R^2 - (hu^2)_L^w - \frac{1}{2}gh_L^{w^2} + \frac{1}{2}g(h_L^w + h_R)(b_R - b_L^w), \end{cases}$$

and s^p are the speeds and $(\cdot)^w$ stands for the quantity in the ghost cell. By using (3.10), we get

$$\left[\begin{matrix} \beta^1 + \gamma^1 \\ \beta^4 + \gamma^2 \end{matrix} \right] = \frac{1}{s^4 - s^1} \left[\begin{matrix} s^4(\delta_1^R + \delta_1^L) - (\delta_2^R + \delta_2^L) \\ -s^1(\delta_1^R + \delta_1^L) + (\delta_2^R + \delta_2^L) \end{matrix} \right].$$

From (3.13) and (3.16), to have

$$\begin{bmatrix} \beta^1 + \gamma^1 \\ \beta^4 + \gamma^2 \end{bmatrix} = \begin{bmatrix} \beta^1_* \\ \beta^2_* \end{bmatrix},$$

we need to ensure

$$(3.17) \qquad \begin{bmatrix} h_L^w \\ (hu^2)_L^w + \frac{1}{2}gh_L^{w^2} \\ (h_L + h_R^w)(b_R^w - b_L) + (h_L^w + h_R)(b_R - b_L^w) \end{bmatrix} = \begin{bmatrix} h_R^w \\ (hu^2)_R^w + \frac{1}{2}gh_R^{w^2} \\ (h_L + h_R)(b_R - b_L) \end{bmatrix}.$$

One approximation is to set the ghost cell state to

(3.18)
$$\begin{bmatrix} h_L^w \\ (hu)_L^w \\ u_L^w \\ b_L^w \end{bmatrix} = \begin{bmatrix} h_R^w \\ (hu)_R^w \\ u_R^w \\ b_R^w \end{bmatrix} = \begin{bmatrix} \frac{1}{2}(h_L + h_R) \\ \frac{1}{2}((hu)_L + (hu)_R) \\ \frac{(hu)_L + (hu)_R}{h_L + h_R} \\ \frac{1}{2}(b_L + b_R) \end{bmatrix}.$$

It is not hard to verify that (3.18) holds as

$$\beta^{1} + \gamma^{1} = \frac{1}{s^{4} - s^{1}} [\beta^{1}(s^{4} - s^{1}) + \beta^{2}(s^{4} - s^{2}) + \beta^{3}(s^{4} - s^{3})]$$

$$= \frac{1}{s^{4} - s^{1}} \left[\frac{s^{4} - s^{1}}{s^{2} - s^{1}} (s^{2}\delta_{1}^{L} - \delta_{2}^{L}) + \frac{s^{4} - s^{2}}{s^{2} - s^{1}} (-s^{1}\delta_{1}^{L} + \delta_{2}^{L}) + \frac{s^{4} - s^{3}}{s^{4} - s^{3}} (s^{4}\delta_{1}^{R} - \delta_{2}^{R}) \right]$$

$$= \frac{1}{s^{4} - s^{1}} [s^{4}(\delta_{1}^{R} + \delta_{1}^{L}) - (\delta_{2}^{R} + \delta_{2}^{L})]$$

and

$$\beta^{4} + \gamma^{2} = \frac{1}{s^{4} - s^{1}} [\beta^{2}(s^{2} - s^{1}) + \beta^{3}(s^{3} - s^{1}) + \beta^{4}(s^{4} - s^{1})]$$

$$= \frac{1}{s^{4} - s^{1}} \left[\frac{s^{2} - s^{1}}{s^{2} - s^{1}} (-s^{1}\delta_{1}^{L} - \delta_{2}^{L}) + \frac{s^{3} - s^{1}}{s^{4} - s^{3}} (s^{4}\delta_{1}^{R} - \delta_{2}^{R}) + \frac{s^{4} - s^{1}}{s^{4} - s^{3}} (-s^{3}\delta_{1}^{R} + \delta_{2}^{R}) \right]$$

$$= \frac{1}{s^{4} - s^{1}} [-s^{1}(\delta_{1}^{R} + \delta_{1}^{L}) + (\delta_{2}^{R} + \delta_{2}^{L})].$$

Note that these averages will preserve the lake at rest case as long as a well-balanced Riemann solver is being used.

3.4. The general case: Interaction from both sides of the barrier. This section combines all of the methods above with a new one, the large time-stepping (LTS) method, to address the most general case of a barrier being overtopped from both sides and the barrier not being aligned with the grid. Unfortunately, the previous methods as designed up until now do not provide a full specification for the averages needed for the h-box method and therefore are insufficient. Instead, we will introduce the LTS method as a means for providing these averages.

The first LTS methods were proposed by LeVeque in a series of papers [17, 18] that generalized the Godunov method to arbitrary Courant numbers. One of the LTS schemes described uses exact or approximate Riemann solvers and wave tracking. It is natural to extend the LTS to our case and add proper approximate wave interactions.

The barrier within a grid cell shown in Figure 7 divides a regular cell into two small cells. The h-box averages $Q^L_{i+1/2}$ and $Q^R_{i+1/2}$ at edge i+1/2 are calculated, and the two waves $\mathcal{Z}^1_{i+1/2}$ and $\mathcal{Z}^2_{i+1/2}$ correspondingly are solved using wave redistribution. However, the waves from edges i-1/2 and i+1/2 may reach the barrier before a full time step is taken and must take into account the barrier's effect. One possible solution to the problem is to keep tracking the waves from these edges, solving for the interaction of the waves with the barrier at each collision. To simplify the computation of these waves that reach the barrier, we will update the h-box cells $Q^L_{i+1/2}$ and $Q^R_{i+1/2}$ and the original wave that reached the barrier will be replaced by two new waves propagating from i+1/2 over the remaining time.

To better present the process, an example is provided in Figure 7. Assume subcritical conditions at each edge at the beginning of the time step. The model problem in one space dimension has a wall (solid bold line) separating a cell into two parts with mesh widths $\alpha \Delta x$ and $(1 - \alpha)\Delta x$. One important property of this method is that as $\alpha \to 0$ the method again limits to the uniform grid case with a barrier at a grid cell edge. Here is an outline of the proposed method in one dimension with the details in Appendix A:

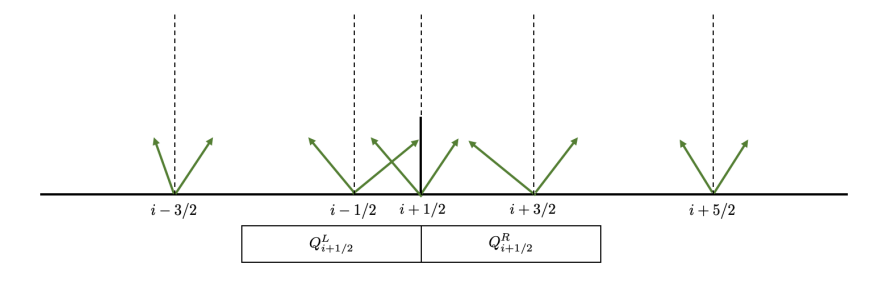


Fig. 7. Step 1: Calculate h-boxes $Q_{i+1/2}^L$ and $Q_{i+1/2}^R$. The model problem in one space dimension has a wall (solid bold line) separating a cell into two parts with mesh widths $\alpha \Delta x$ and $(1-\alpha)\Delta x$. The boxes below the axis indicate the h-boxes used to compute the flux at the interface i+1/2.

1. Compute the cell averages $Q_{i+1/2}^L$ and $Q_{i+1/2}^R$ in the h-boxes adjoining each cell interface $x_{i+1/2}$. This is done using weighted sums of the reconstructed values on the underlying nonuniform grid.

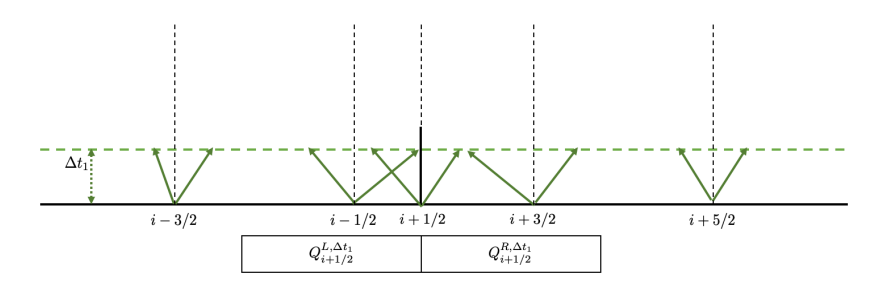


Fig. 8. Step 2: at Δt_1 , the wave $\mathcal{Z}^2_{i-1/2}$ reaches the barrier. Update $Q^L_{i+1/2}$ and $Q^R_{i+1/2}$.

2. Compute the first arrival time Δt_1 .¹ Update $Q_{i+1/2}^L$ and $Q_{i+1/2}^R$ using (A.2) and (A.3), respectively.

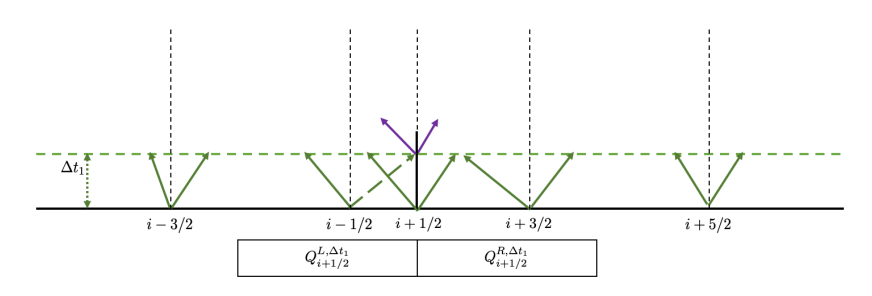


FIG. 9. Step 3: at Δt_1 , replace $\mathcal{Z}^2_{i-1/2}$ with $\mathcal{Z}^{1,\Delta t_1}_{i+1/2}$ and $\mathcal{Z}^{2,\Delta t_1}_{i+1/2}$ at interface i+1/2 using updated $Q^{L,\Delta t_1}_{i+1/2}$ and $Q^{R,\Delta t_1}_{i+1/2}$.

3. Determine waves $\mathcal{Z}_{i+1/2}^{L,\Delta t_1}$ and $\mathcal{Z}_{i+1/2}^{R,\Delta t_1}$ at $x_{i+1/2}$ based on the cell averages $Q_{i+1/2}^{L,\Delta t_1}$ and $Q_{i+1/2}^{R,\Delta t_1}$ as in Figure 9.

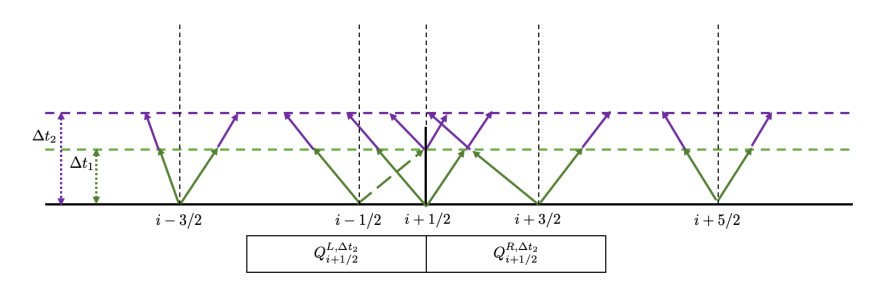


Fig. 10. Step 4: at Δt_2 , the wave $\mathcal{Z}^1_{i+3/2}$ reaches the barrier. Update $Q^{L,\Delta t_1}_{i+1/2}$ and $Q^{R,\Delta t_1}_{i+1/2}$.

- 4. Compute the second arrival time Δt_2 . Update $Q_{i+1/2}^{L,\Delta t_1}$ and $Q_{i+1/2}^{R,\Delta t_1}$ using (A.4) and (A.5).
- 5. Determine waves $\mathcal{Z}_{i+1/2}^{L,\Delta t_2}$ and $\mathcal{Z}_{i+1/2}^{R,\Delta t_2}$ at $x_{i+1/2}$ based on the cell averages $Q_{i+1/2}^{L,\Delta t_2}$ and $Q_{i+1/2}^{R,\Delta t_2}$ as in Figure 11.

¹Under the setting of this example, $\Delta t_1 = \min\left(\frac{\alpha \Delta x}{s_{i-1/2}^2}, -\frac{(1-\alpha)\Delta x}{s_{i+1/2}^1}\right)$. For more details about the time step updates, we refer the reader to the PyClaw library https://github.com/jillelee/pyclaw.

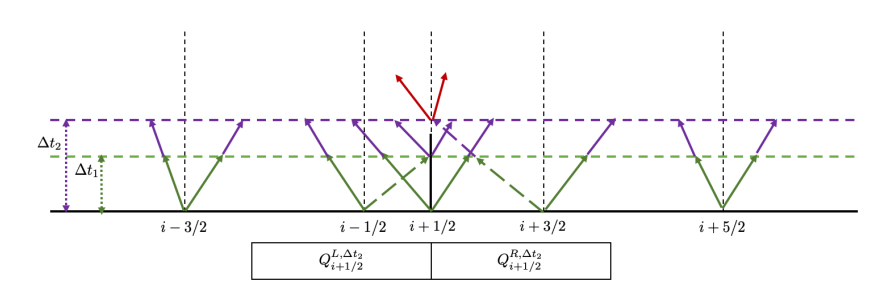


Fig. 11. Step 5: at Δt_2 , replace $\mathcal{Z}^1_{i+3/2}$ with $\mathcal{Z}^{1,\Delta t_2}_{i+1/2}$ and $\mathcal{Z}^{2,\Delta t_2}_{i+1/2}$ at interface i+1/2 using updated $Q^{L,\Delta t_2}_{i+1/2}$ and $Q^{R,\Delta t_2}_{i+1/2}$.

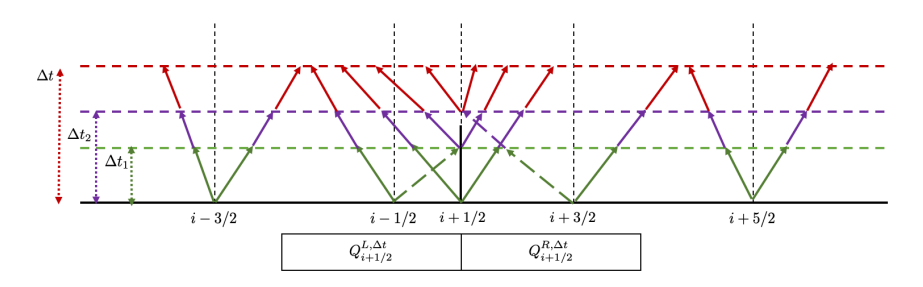


Fig. 12. Step 6: at Δt , update $Q_{i-1}^{\Delta t}$, $Q_{i}^{\Delta t}$, $Q_{i+1}^{\Delta t}$, and $Q_{i+2}^{\Delta t}$ accordingly.

6. Update
$$Q_{i-1}^{\Delta t},\,Q_{i}^{\Delta t},\,Q_{i+1}^{\Delta t},\,$$
 and $Q_{i+2}^{\Delta t}$ using (A.6), (A.7), (A.8) and (A.9).

- 4. Numerical results. This section details numerical results that test the methods described above for conservation and robustness, including the dynamics of the wet-dry interfaces along with the flexibility of placing a barrier that is not aligned with the grid. In all these cases, the value of Δt is constrained by the large grid cells rather than the cells containing the barriers. The code that has implemented these results is available online from https://github.com/jillelee/hbox-examples using PyClaw https://github.com/jillelee/pyclaw. For all the examples, variable time steps were taken, constrained by the global CFL condition multiplied by 0.8. Spatial resolution was set to 50 cells, resulting in $\Delta x = 0.04$.
- **4.1.** Well-balancing and the ghost fluid. Given the importance of well-balancing, the first test case aims to demonstrate that well-balancing is retained. For this test case, the bathymetry is set to

$$(4.1) b(x) = -0.6 + 0.2x, -1 \le x \le 1,$$

with the depth set to h(x) = -b(x) corresponding to a flat surface. The wall is at x = 0.0 with a height of 0.35. The initial velocity is zero everywhere so that the surface should remain undisturbed. We present the results of two different approaches to setting the ghost cell. Adopting the notation in subsection 3.3, one approach is represented by (3.18) (see Figures 13a and 13b), while an alternative approach is

obtained by setting the ghost cell to

$$\begin{bmatrix}
h_L^w \\ (hu)_L^w \\ u_L^w \\ b_L^w
\end{bmatrix} = \begin{bmatrix}
0 \\ 0 \\ 0 \\ b_R
\end{bmatrix},
\begin{bmatrix}
h_R^w \\ (hu)_R^w \\ u_R^w \\ b_R^w
\end{bmatrix} = \begin{bmatrix}
0 \\ 0 \\ 0 \\ b_L
\end{bmatrix},$$

resulting in Figures 13c and 13d. As seen in Figure 13c, a disturbance appears around the barrier despite a steady state being maintained. This leads us to believe that (3.18) leads to more robust results.

4.2. High barriers. This test case demonstrates that the barrier does indeed keep water from flowing past it provided that the barrier is high enough. The initial conditions are

$$\begin{cases} h(x,0) = 1.2 & \text{if } x \le -0.2, \\ h(x,0) = 0.8 & \text{otherwise,} \end{cases} \quad hu(x,0) = 0.0, \ b(x) = -0.8, \ -1 \le x \le 1,$$

and the boundary conditions at $x=\pm 1$ are wall boundaries. The wall is placed at x=-0.024 within a cell, and the wall height is 1.5. In Figure 14, the left panel presents the entire domain and the right panel shows zoomed-in plots. For each subplot in Figure 14a, the upper plot is the plot of depth (h(x,t)) and the lower is the plot of momentum (hu(x,t)). As shown in the right panel of Figure 14, the barrier separates a regular cell into two parts with sizes $\alpha\Delta x$ and $(1-\alpha)\Delta x$, where $\alpha=0.4$. With a zero momentum initially, there is a jump in the depth of the fluid at x=-0.2 as shown in Figure 14a. At t=0.1s, Figure 14c shows a wave that cannot overcome the barrier and reflects off of the barrier instead. The right side of the barrier shows no perturbation for all time, demonstrating that no water overcomes the barrier. Since the maintenance of the steady state at any given grid resolution and barrier placement is critical for modeling, this case is presented to show that the Riemann solver maintains this property.

4.3. An overtopped barrier on a sloping beach. The final test case matches a more realistic setting for coastal flood modeling. In this case, an incoming wave has enough momentum so that the wave overtops the barrier and leads to flooding on the other side of the barrier. Figure 15 presents an example with a sloping bathymetry and wet-dry interface. The bathymetry is a simple idealization of a near-shore ocean basin with initial conditions

(4.4)
$$\begin{cases} h(x,0) = 0.4 - b(x) & \text{if } x \le -0.2, \\ h(x,0) = -b(x) & \text{if } -0.2 < x \le -0.024, \\ h(x,0) = 0.0 & \text{otherwise,} \end{cases}$$

and

$$hu(x,0) = 0.0, \quad b(x) = -0.6 + 0.2x, \quad -1 < x < 1,$$

with wall boundary conditions at $x = \pm 1$. The wall is placed at x = -0.024 within a cell, and the wall height is 0.8. As shown in Figure 15a, the right side to the barrier is initially dry and the jump in the depth of the fluid is located at x = -0.2. The first numerical challenge of this problem is how to robustly and accurately simulate the fluid overcoming the barrier and flooding to the right. Furthermore, the Riemann

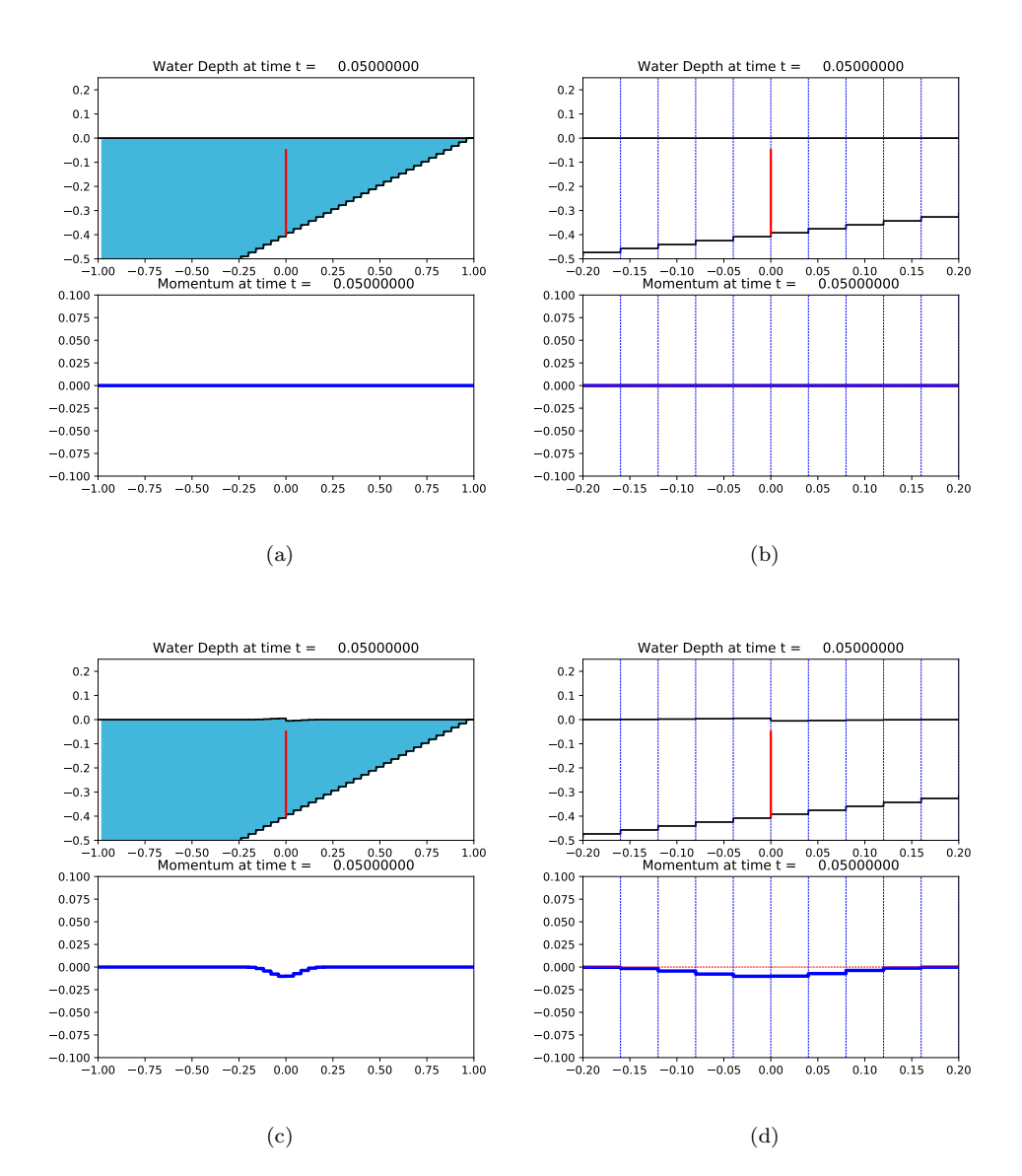


FIG. 13. Comparisons between different settings of the ghost cell. Top: Simulation results with setting (3.18). Bottom: Simulation results with setting (4.2). The initial condition is b(x) = -0.6 + 0.2x with the flat surface h(x) = -b(x). The height of the wall (marked as the red line) is 0.35 at x = 0. The initial velocity is zero so that the surface should remain undisturbed. The right panel is the zoom-in region near the barrier. Color is available online only.

solver needs to deal with the wet-dry interface that represents the moving shoreline during inundation. In Figure 15c, at t=0.15s, the water overtops the barrier and cascades into a dry cell. Eventually, it reaches a steady state in Figure 15e as expected. Mass conservation is maintained to machine precision throughout the simulation.

5. Conclusions and future work. The methods presented and demonstrated provide a means for applying existing shallow water Riemann solvers to scenarios

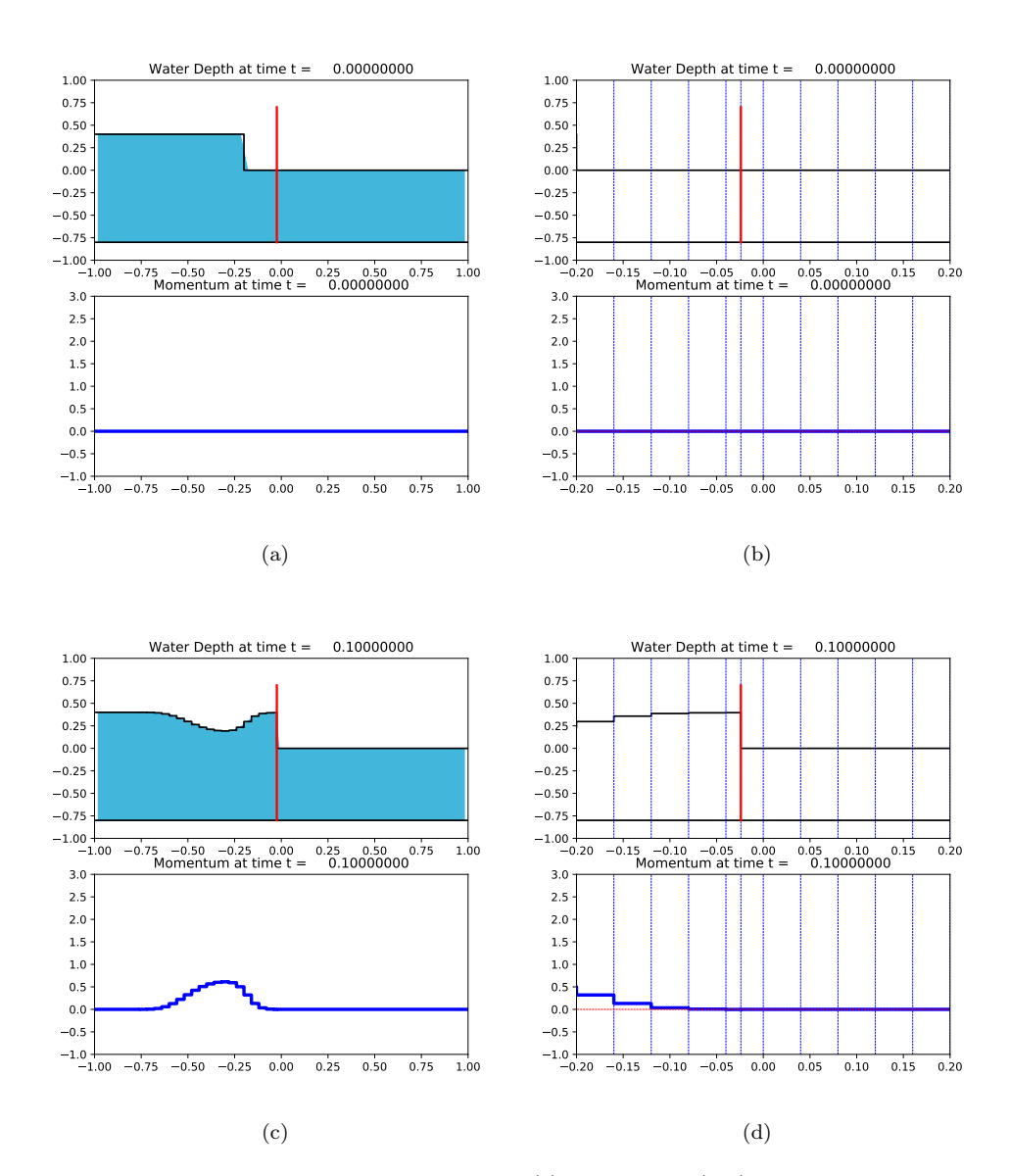


Fig. 14. The initial condition is shown in (a): $\alpha = 0.4$, h(x,0) = 1.2 if x < -0.2 and h(x,0) = 0.8 otherwise, u(x,0) = 0. Wall height is 1.5 and the wave cannot over-top the barrier marked as the red line. The wave is reflected by the barrier after hitting it. The right panel is the zoom-in region near the barrier. Color is available online only.

where a barrier may exist that may not be computationally feasible to resolve. These extensions maintain important properties of the original Riemann solver, such as conservation and well-balancedness, while removing the spatial discretization and resulting CFL constraints. These extensions should also extend to not only other shallow water solvers of a similar flavor but also to other similar systems of conservation laws with similar constraints. Note that the h-box method itself is not just useful in the case of a solid wall embedded in the interior of a domain but rather anytime when

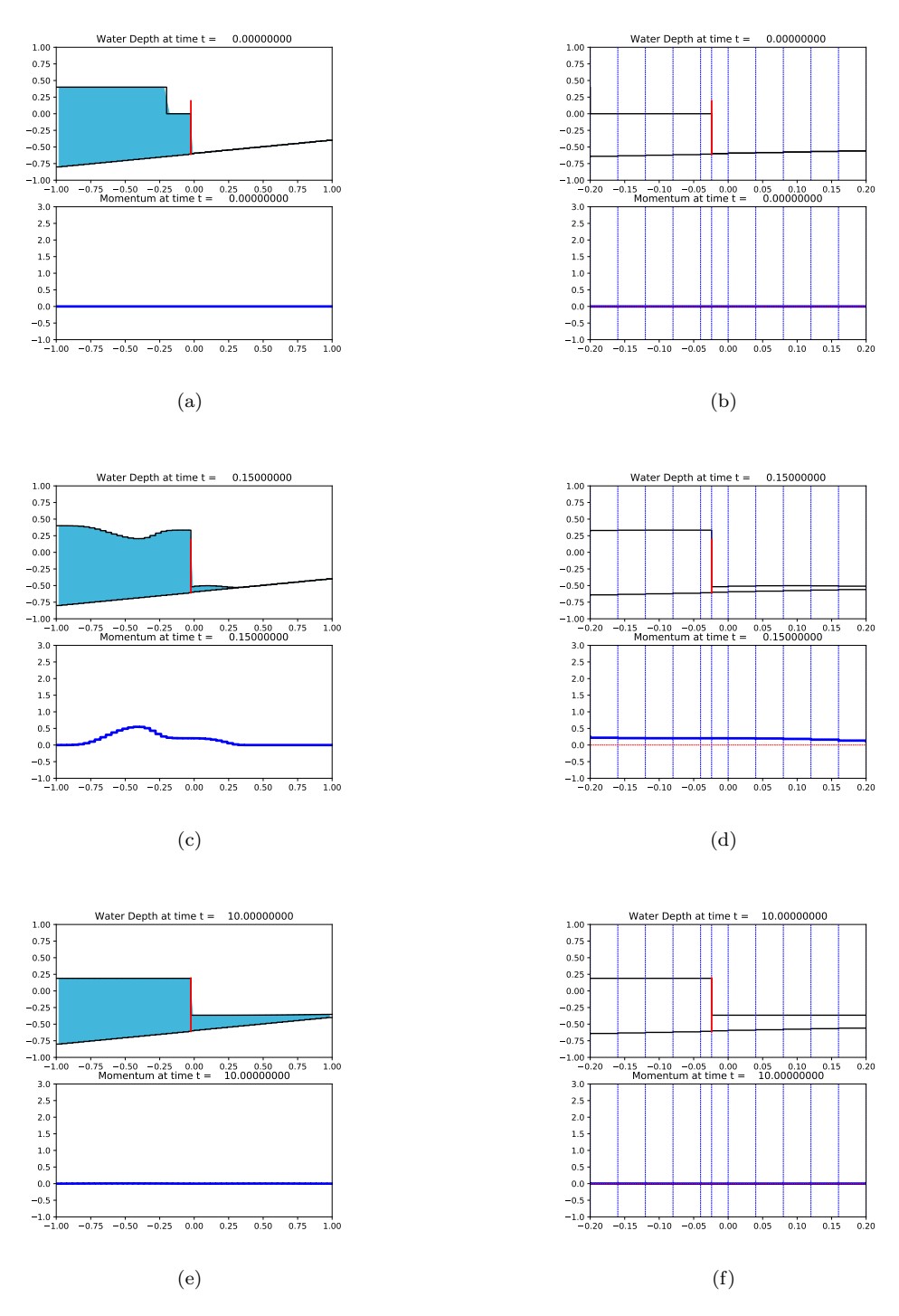


FIG. 15. Simulation of a wave that can overtop the barrier, causing the water to cascade into a dry cell. The piecewise constant plots of h and b present the average value over each cell. The initial condition is shown in (a): bathymetry slope is from -0.8 to -0.4, and u(x,0) = 0. $\eta(x,0) = 0.4$ if $x \le -0.2$; $\eta(x,0) = 0.0$ if $-0.2 < x \le -0.024$ and $\eta(x,0) = b(x)$, where $\eta(x,t) = h(x,t) + b(x)$. Wall height is 0.8 (marked as the red line). The right panel is the zoom-in region near the barrier. Color is available online only.

there is an advantage to having a small cell computationally. These methods demonstrate that with minimal computational effort the CFL constraint can be mitigated and additional effects introduced.

The highest barrier to the use of the methods described for more general use, in particular higher dimensions, is the complexity of the most general case as described and the use of the LTS method. Because of this, finding a way to either reduce the complexity of the LTS method or to find an alternative to the LTS method is the highest priority for future work. Other future directions include the full extension to two dimensions, continued analysis of the convergence properties of the proposed method, the addition of adaptive mesh refinement, and exploration into extending h-boxes to the multi-h-box case, possibly alleviating the CFL condition in other cases, such as spatially localized, fast wave speeds or other CFL constraints.

Appendix A. Modified h-box intermediate quantities. In this section, we provide the details of the intermediate quantity updates under the setting in subsection 3.4. In step 2 shown as Figure 8, Δt_1 is the earlier arrival time of the waves, which are the right-moving wave from edge i - 1/2 and the left-moving wave from edge i + 1/2. Therefore,

(A.1)
$$\Delta t_1 = \min\left(\frac{\alpha \Delta x}{s_{i-1/2}^2}, -\frac{(1-\alpha)\Delta x}{s_{i+1/2}^1}\right).$$

At the first arrival time, Δt_1 , $Q_{i+1/2}^L$, and $Q_{i+1/2}^R$ are updated as

$$\begin{split} Q_{i+1/2}^{L,\Delta t_1} &= Q_{i+1/2}^L - \frac{\Delta t_1}{\Delta x} (\mathcal{Z}_{i-1/2}^2 + \mathcal{Z}_{i+1/2}^1) \\ &- \frac{\Delta t_1}{\Delta x} \bigg(\frac{\min\{-s_{i-1/2}^1 \Delta t_1, (1-\alpha) \Delta x\}}{-s_{i-1/2}^1 \Delta t_1} \mathcal{Z}_{i-1/2}^1 \\ &+ \frac{\max\{0, s_{i-3/2}^2 \Delta t_1 - \alpha \Delta x\}}{s_{i-3/2}^2 \Delta t_1} \mathcal{Z}_{i-3/2}^2 \bigg), \end{split}$$

$$\begin{aligned} Q_{i+1/2}^{R,\Delta t_1} &= Q_{i+1/2}^R - \frac{\Delta t_1}{\Delta x} (\mathcal{Z}_{i+1/2}^2 + \mathcal{Z}_{i+3/2}^1) \\ &- \frac{\Delta t_1}{\Delta x} \bigg(\frac{\min\{s_{i+3/2}^2 \Delta t_1, \alpha \Delta x\}}{s_{i+3/2}^2 \Delta t_1} \mathcal{Z}_{i+3/2}^2 \\ &+ \frac{\max\{0, -s_{i+5/2}^2 \Delta t_1 - (1 - \alpha)\Delta x\}}{-s_{i+5/2}^2 \Delta t_1} \mathcal{Z}_{i+5/2}^1 \bigg). \end{aligned}$$

Similarly, at the second arrival time Δt_2 (see Figure 10), update $Q_{i+1/2}^{L,\Delta t_1}$ and $Q_{i+1/2}^{R,\Delta t_1}$ as

$$\begin{split} Q_{i+1/2}^{L,\Delta t_2} &= Q_{i+1/2}^L - \frac{\Delta t_1}{\Delta x} (\mathcal{Z}_{i-1/2}^2) - \frac{\Delta t_2}{\Delta x} (\mathcal{Z}_{i+1/2}^1) - \frac{\Delta t_2 - \Delta t_1}{\Delta x} (\mathcal{Z}_{i+1/2}^{1,\Delta t_1}) \\ &- \frac{\Delta t_2}{\Delta x} \left(\frac{\min\{-s_{i-1/2}^1 \Delta t_2, (1-\alpha)\Delta x\}}{-s_{i-1/2}^1 \Delta t_2} \mathcal{Z}_{i-1/2}^1 \right. \\ &+ \frac{\max\{0, s_{i-3/2}^2 \Delta t_2 - \alpha \Delta x\}}{s_{i-3/2}^2 \Delta t_2} \mathcal{Z}_{i-3/2}^2 \right), \end{split}$$

$$\begin{aligned} Q_{i+1/2}^{R,\Delta t_2} &= Q_{i+1/2}^R - \frac{\Delta t_2}{\Delta x} (\mathcal{Z}_{i+1/2}^2 + \mathcal{Z}_{i+3/2}^1) - \frac{\Delta t_2 - \Delta t_1}{\Delta x} (\mathcal{Z}_{i+1/2}^{2,\Delta t_1}) \\ &- \frac{\Delta t_2}{\Delta x} \left(\frac{\min\{s_{i+3/2}^2 \Delta t_2, \alpha \Delta x\}}{s_{i+3/2}^2 \Delta t_2} \mathcal{Z}_{i+3/2}^2 \right. \\ &+ \frac{\max\{0, -s_{i+5/2}^2 \Delta t_2 - (1 - \alpha) \Delta x\}}{-s_{i+5/2}^2 \Delta t_2} \mathcal{Z}_{i+5/2}^1 \right). \end{aligned}$$

At last, update all of the cells $Q_{i-1}^{\Delta t}$, $Q_i^{\Delta t}$, $Q_{i+1}^{\Delta t}$, and $Q_{i+2}^{\Delta t}$ in Figure 12 as

$$Q_{i-1}^{\Delta t} = Q_{i-1} - \frac{\Delta t}{\Delta x} \left(Z_{i-3/2}^2 + Z_{i-1/2}^1 + \frac{\max\{0, -s_{i+1/2}^1 \Delta t - \alpha \Delta x\}}{-s_{i+1/2}^1 \Delta t} Z_{i+1/2}^1 \right)$$

$$(A.6) - \frac{\Delta t - \Delta t_1}{\Delta x} \left(\frac{\max\{0, -s_{i+1/2}^1 (\Delta t - \Delta t_1) - \alpha \Delta x\}}{-s_{i+1/2}^1 (\Delta t - \Delta t_1) - \alpha \Delta x} Z_{i+1/2}^1 \right)$$

$$- \frac{\Delta t - \Delta t_2}{\Delta x} \left(\frac{\max\{0, -s_{i+1/2}^{1,\Delta t_1} (\Delta t - \Delta t_1) - \alpha \Delta x\}}{-s_{i+1/2}^{1,\Delta t_2} (\Delta t - \Delta t_2)} Z_{i+1/2}^{1,\Delta t_2} \right),$$

$$Q_i^{\Delta t} = Q_i - \frac{\Delta t_1}{\alpha \Delta x} (Z_{i-1/2}^2) - \frac{\Delta t}{\alpha \Delta x} \left(\frac{\min\{-s_{i+1/2}^{1,\Delta t_1} (\Delta t - \Delta t_2) - \alpha \Delta x\}}{-s_{i+1/2}^1 (\Delta t - \Delta t_1)} Z_{i+1/2}^{1,\Delta t_1} \right)$$

$$- \frac{\Delta t - \Delta t_1}{\alpha \Delta x} \left(\frac{\min\{-s_{i+1/2}^{1,\Delta t_1} (\Delta t - \Delta t_1), \alpha \Delta x\}}{-s_{i+1/2}^1 (\Delta t - \Delta t_1)} Z_{i+1/2}^{1,\Delta t_1} \right)$$

$$- \frac{\Delta t - \Delta t_2}{\alpha \Delta x} \left(\frac{\min\{-s_{i+1/2}^{1,\Delta t_1} (\Delta t - \Delta t_1), \alpha \Delta x\}}{-s_{i+1/2}^1 (\Delta t - \Delta t_2)} Z_{i+1/2}^{1,\Delta t_2} \right),$$

$$Q_{i+1}^{\Delta t} = Q_{i+1} - \frac{\Delta t_2}{(1 - \alpha) \Delta x} (Z_{i+3/2}^1)$$

$$- \frac{\Delta t}{(1 - \alpha) \Delta x} \left(\frac{\min\{s_{i+1/2}^2 (\Delta t - \Delta t_2), \alpha \Delta x\}}{s_{i+1/2}^2 (\Delta t - \Delta t_2)} Z_{i+1/2}^{2,\Delta t_1} \right)$$

$$- \frac{\Delta t - \Delta t_1}{(1 - \alpha) \Delta x} \left(\frac{\min\{s_{i+1/2}^2 (\Delta t - \Delta t_1), (1 - \alpha) \Delta x\}}{s_{i+1/2}^2 (\Delta t - \Delta t_1)} Z_{i+1/2}^{2,\Delta t_1} \right)$$

$$- \frac{\Delta t - \Delta t_2}{(1 - \alpha) \Delta x} \left(\frac{\min\{s_{i+1/2}^2 (\Delta t - \Delta t_1), (1 - \alpha) \Delta x\}}{s_{i+1/2}^2 (\Delta t - \Delta t_2)} Z_{i+1/2}^{2,\Delta t_2} \right),$$

$$Q_{i+2}^{\Delta t} = Q_{i+2} - \frac{\Delta t}{\Delta x} \left(Z_{i+3/2}^2 + Z_{i+5/2}^1 \right)$$

$$+ \frac{\max\{0, s_{i+1/2}^2 (\Delta t - \Delta t_2), (1 - \alpha) \Delta x\}}{s_{i+1/2}^2 (\Delta t - \Delta t_1)} Z_{i+1/2}^{2,\Delta t_1} \right),$$

$$Q_{i+2}^{\Delta t} = Q_{i+2} - \frac{\Delta t}{\Delta x} \left(Z_{i+3/2}^2 + Z_{i+5/2}^1 \right)$$

$$- \frac{\Delta t - \Delta t_1}{\Delta x} \left(\frac{\max\{0, s_{i+1/2}^2 (\Delta t - \Delta t_1) - (1 - \alpha) \Delta x\}}{s_{i+1/2}^2 (\Delta t - \Delta t_1)} Z_{i+1/2}^{2,\Delta t_1} \right)$$

$$- \frac{\Delta t - \Delta t_1}{\Delta x} \left(\frac{\max\{0, s_{i+1/2}^2 (\Delta t - \Delta t_2) - (1 - \alpha) \Delta x\}}{s_{i+1/2}^2 (\Delta t - \Delta t_1)} Z_{i+1/2}^{2,\Delta t_1} \right)$$

$$- \frac{\Delta t - \Delta t_2}{\Delta x} \left(\frac{\max\{0, s_{i+1/2}^2 (\Delta t - \Delta t_2) - (1 - \alpha) \Delta x\}}{s_{i+1/2}^2 (\Delta t - \Delta t_2)} Z_{i+1/2}^{2,\Delta t_1} \right)$$

$$- \frac{\Delta t - \Delta t_2}{\Delta x} \left(\frac{\max\{0, s_{i+1/2}^2 (\Delta t - \Delta t_2) - (1 - \alpha) \Delta x\}}{s_{i+1/2}^2 (\Delta t - \Delta t_2)} Z_{i+1/2}^{2,\Delta t_2} \right)$$

$$- \frac{\Delta t - \Delta t_2}{\Delta x}$$

REFERENCES

- D. S. Bale, R. J. Leveque, S. Mitran, and J. A. Rossmanith, A wave propagation method for conservation laws and balance laws with spatially varying flux functions, SIAM J. Sci. Comput., 24 (2002), pp. 955–978, https://doi.org/10.1137/S106482750139738X.
- [2] S. BAYYUK AND K. POWELL, A simulation technique for 2-d unsteady inviscid flows around arbitrarily moving and deforming bodies of arbitrary geometry, in Proceedings of the 11th Computational Fluid Dynamics Conference, 1993.
- M. Berger and C. Helzel, A simplified h-box method for embedded boundary grids, SIAM J. Sci. Comput., 34 (2012), pp. A861–A888, https://doi.org/10.1137/110829398.
- [4] M. BERGER AND R. LEVEQUE, An adaptive Cartesian mesh algorithm for the Euler equations in arbitrary geometries, in Proceedings of the 9th Computational Fluid Dynamics Conference, 1989.
- [5] M. Berger and R. Leveque, Cartesian meshes and adaptive mesh refinement for hyperbolic partial differential equations, in Proceedings of the Third International Conference on Hyperbolic Problems, Uppsala, Sweden, 1990.
- [6] M. J. BERGER, C. HELZEL, AND R. J. LEVEQUE, h-box methods for the approximation of hyperbolic conservation laws on irregular grids, SIAM J. Numer. Anal., 41 (2003), pp. 893– 918, https://doi.org/10.1137/S0036142902405394.
- [7] M. J. BERGER AND R. J. LEVEQUE, Stable boundary conditions for cartesian grid calculations, Comput. Syst. Eng., 1 (1990), pp. 305–311.
- [8] M. J. Berger and R. J. Leveque, A Rotated Difference Scheme for Cartesian Grids in Complex Geometries, AIAA Paper CP-91-1602, 1991, pp. 1-9.
- [9] I.-L. CHERN AND P. COLELLA, A Conservative Front Tracking Method for Hyperbolic Conservation Laws, LLNL Report UCRL-97200, Lawrence Livermore National Laboratory, Livermore, CA, 1987.
- [10] W. Coirier and K. Powell, An accuracy assessment of Cartesian-mesh approaches for the Euler equations, in Proceedings of the 11th Computational Fluid Dynamics Conference, 1993.
- [11] P. COLELLA, D. T. GRAVES, B. J. KEEN, AND D. MODIANO, A Cartesian grid embedded boundary method for hyperbolic conservation laws, J. Comput. Phys., 211 (2006), pp. 347–366.
- [12] A. DADONE AND B. GROSSMAN, Ghost-cell method for analysis of inviscid three-dimensional flows on cartesian-grids, Comput. & Fluids, 36 (2007), pp. 1513–1528.
- [13] J. FALCOVITZ, G. ALFANDARY, AND G. HANOCH, A two-dimensional conservation laws scheme for compressible flows with moving boundaries, J. Comput. Phys., 138 (1997), pp. 83–102.
- [14] H. FORRER AND R. JELTSCH, A higher-order boundary treatment for Cartesian-grid methods, J. Comput. Phys., 140 (1998), pp. 259–277.
- [15] D. L. GEORGE, Augmented Riemann solvers for the shallow water equations over variable topography with steady states and inundation, J. Comput. Phys., 227 (2008), pp. 3089– 3113.
- [16] B. GUSTAFSSON, H.-O. KREISS, AND A. SUNDSTRÖM, Stability theory of difference approximations for mixed initial boundary value problems. II., Math. Comp., 26 (1972), pp. 649–686.
- [17] R. J. LEVEQUE, Large time step shock-capturing techniques for scalar conservation laws, SIAM J. Numer. Anal., 19 (1982), pp. 1091–1109, https://doi.org/10.1137/0719080.
- [18] R. J. LEVEQUE, A large time step generalization of Godunov's method for systems of conservation laws, SIAM J. Numer. Anal., 22 (1985), pp. 1051–1073, https://doi.org/10.1137/0722063.
- [19] E. MAS, J. BRICKER, S. KURE, B. ADRIANO, C. YI, A. SUPPASRI, AND S. KOSHIMURA, Field survey report and satellite image interpretation of the 2013 Super Typhoon Haiyan in the Philippines, Nat. Hazards Earth Syst. Sci., 15 (2015), pp. 805–816.
- [20] A. Parris, P. Bromirski, V. Burkett, D. R. Cayan, M. Culver, J. Hall, R. Horton, K. Knuuti, R. Moss, J. Obeysekera, A. Sallenger, and J. Weiss, Global Sea Level Rise Scenarios for the United States National Climate Assessment, NOAA Technical Report OAR CPO-1, 2012.
- [21] R. B. Pember, J. B. Bell, P. Colella, W. Y. Curtchfield, and M. L. Welcome, An adaptive Cartesian grid method for unsteady compressible flow in irregular regions, J. Comput. Phys., 120 (1995), pp. 278–304.
- [22] J. J. Quirk, An alternative to unstructured grids for computing gas dynamic flows around arbitrarily complex two-dimensional bodies, Comput. & Fluids, 23 (1994), pp. 125–142.
- [23] A. B. SMITH AND R. W. KATZ, US billion-dollar weather and climate disasters: Data sources, trends, accuracy and biases, Nat. Hazards (Dordr.), 67 (2013), pp. 387–410.

- [24] T. STOCKER, Climate Change 2013: The Physical Science Basis: Working Group I Contribution to the Fifth Assessment Report of the Intergovernmental Panel on Climate Change, Cambridge University Press, Cambridge, UK/New York, 2014.
- [25] S. Xu, T. Aslam, and D. S. Stewart, High resolution numerical simulation of ideal and nonideal compressible reacting flows with embedded internal boundaries, Combust. Theory Model., 1 (1997), pp. 113–142.